Nanoscale

PAPER

View Article Online
View Journal | View Issue

Cite this: *Nanoscale*, 2025, **17**, 25727

Enhanced valley polarization in MoS_2 *via* substrate-induced strain and transition dipole moment modulation

Ashish Soni,[a,b,f] Nagendra S. Kamath,[a,b] Fathima IS,[c] Yun-Yang Shen,[d] Wen-Hao Chang,[d,e] Abir De Sarkar[c] and Suman Kalyan Pal*[a,b]

Monolayer transition metal dichalcogenides (TMDs) are promising materials for valleytronic and quantum photonic applications due to their valley-selective optical transitions. However, tailoring and enhancing valley polarization remains a challenge, particularly under ambient conditions. Here, we present a comprehensive helicity-resolved femtosecond transient absorption spectroscopy (HR-TAS) study of large-area monolayer MoS_2, comparing the as-grown and substrate-transferred samples to uncover the impact of strain and defect engineering on valley depolarization dynamics. Our measurements reveal that the degree of polarization (DOP) and the valley lifetime are significantly enhanced in transferred MoS_2, with a pronounced dependence on excitation fluence and temperature. We attribute this enhancement to a combination of strain-induced symmetry breaking, defect-induced carrier localization, and reduced intervalley scattering *via* the Maialle–Silva–Sham mechanism. Supported by first-principles calculations, we identify a novel contribution from spin-dependent transition dipole moments (TDMs), which further boosts valley selectivity in strained MoS_2 on quartz substrates. This study provides an experimental and theoretical correlation of TDM modulation with enhanced valley polarization in transferred MoS_2. Our findings offer a pathway to enable new design principles for spin–valley-coupled optoelectronics applications through substrate and strain engineering.

Received 11th July 2025,
Accepted 6th October 2025

DOI: 10.1039/d5nr02938d

rsc.li/nanoscale

Introduction

The search for next-generation quantum systems that will enhance the current device capabilities is an area of focus in the present day. Transition metal dichalcogenides (TMDs), a family of two-dimensional (2D) materials, have been recognized as prominent candidates for such systems. TMDs exhibit a direct bandgap in the monolayer regime with strong spin–orbit coupling (SOC), inversion symmetry breaking,[1–3] and fascinating spin valley locking.[4,5] As a consequence of these unique properties, TMDs display the presence of spin polarized bands at the K points of the Brillouin zone that are termed valleys. Evidence of valleys was first demonstrated by polarization-dependent photoluminescence (PL).[6–8] The combination of valleys and spin polarization opens up a new paradigm of valleytronics, which, like electronics and spintronics, offers potential to store and encode quantum information. The valley polarization of TMDs can be generated and quantified with the help of helicity-resolved optical excitation.[6,7] Optical selection rules related to valley and spin polarization allow the rapid manipulation of valleytronic devices by optical pumping.[9,10] TMD-based electronic devices such as transistors,[11] solar devices,[12–14] and p–n junctions[15,16] have already been explored from various aspects. However, the practical realization of future spin- and valleytronic devices based on TMDs is yet to be fully achieved. Understanding the depolarization mechanism is crucial for the application of TMDs in designing valleytronic devices. Time-resolved photoluminescence (TRPL) and time-resolved Kerr rotation have previously been utilized to determine the physical origin of valley polarization and depolarization phenomena.[17–19]

In the realm of valleytronics, understanding the mechanisms governing valley depolarization in monolayer TMDs is of paramount importance. Previous studies have extensively explored the D'yakonov–Perel' (DP) and Elliott–Yafet (EY)

[a]*School of Physical Sciences, Indian Institute of Technology Mandi, Kamand, Mandi 175005, Himachal Pradesh, India. E-mail: suman@iitmandi.ac.in*
[b]*Advanced Materials Research Centre, Indian Institute of Technology Mandi, Kamand, Mandi 175005, Himachal Pradesh, India*
[c]*Institute of Nano Science and Technology, Knowledge City, Sector 81, Mohali 140306, India*
[d]*Department of Electrophysics, National Yang Ming Chiao Tung University, Hsinchu 30010, Taiwan*
[e]*Research Center for Applied Sciences, Academia Sinica, Nankang, Taipei 11529, Taiwan*
[f]*Department of Chemistry, Emory University, Atlanta, Georgia 30322, USA*

mechanisms as key contributors to valley depolarization *via* spin relaxation.[20,21] The DP mechanism arises from SOC and spin precession in momentum space, leading to the decoherence of valley-polarized carriers. On the other hand, the EY mechanism involves spin–flip scattering events that cause valley depolarization by mixing spin states. These mechanisms, which have garnered significant attention, underscore the intricate interplay between the spin and valley degrees of freedom in TMDs. Recent theoretical and experimental investigations have shed light on the Maialle–Silva–Sham (MSS) mechanism, stemming from the intervalley electron–hole (e–h) exchange interaction, as a potential dominant contributor to spin and valley relaxation phenomena in monolayer MoS_2 and WSe_2.[17,20,22]

Large-area homogeneous monolayers and the selection of suitable substrates are fundamental necessities for device fabrication, as the dielectric medium of the substrate plays a crucial role in the optoelectronic properties of TMDs. It is well established in the literature that transferring monolayer TMDs onto different substrates can alter the surrounding dielectric medium and introduce non-uniform strain throughout the layer.[23] Strategies such as changing the dielectric medium or electric field[24–26] or introducing strain are commonly applied to manipulate the electronic band structure and binding energy of excitons in 2D materials.[27,28] Among them, introducing strain is a well-known technique to modulate the electronic band structure of TMDs. Moreover, strain has been demonstrated to affect the charge dynamics in TMDs, such as exciton to trion conversion[29] and exciton annihilation.[30–32] However, the effect of substrate change and induced non-uniform strain on optoelectronic properties, such as valley polarization and the depolarization mechanism are rarely considered in general experimental studies. The associated valley depolarization dynamics and corresponding excitonic transitions have not been explored much. A detailed survey of substrate dependency and the effect of strain-induced band splitting on valley depolarization dynamics is still lacking. In this work, we present a systematic helicity-resolved femtosecond transient absorption spectroscopy study on large-area monolayer MoS_2, conducted at two different temperatures and across a broad range of excitation fluences. The primary objective of this study is to elucidate the influence of the substrate on excitonic and valley-related properties, particularly valley depolarization dynamics. Additionally, *ab initio* calculations were carried out to gain deeper insight into how substrate-induced effects alter the valley-selective optical behavior of monolayer MoS_2.

Methods

Preparation and transfer of 2D monolayer MoS_2

Large-area monolayer MoS_2 was prepared using the chemical vapor deposition (CVD) technique.[32] Subsequently, the samples were transferred onto various substrates including Si/SiO_2, sapphire, and quartz using the wet transfer technique. A Bruker dimension (Model Icon PT) atomic force microscope (AFM) was then used to measure the thickness of all the samples.

Steady-state absorption, photoluminescence, and Raman spectroscopy

The steady-state absorption spectrum was obtained using a Shimadzu UV-2450 spectrometer (Agilent Technologies, USA). PL and Raman spectra were obtained at room temperature in the back-scattering configuration using an optical microscope. A 532 nm laser was used to illuminate the sample through a 100× objective lens with a numerical aperture (NA) of 0.9. Subsequently, the signals were analyzed using a monochromator employing gratings with 600 lines per mm and 1800 lines per mm for PL and Raman measurements, respectively. Detection of the signals was accomplished using an air-cooled CCD.

Helicity-resolved transient absorption spectroscopy (HR-TAS)

HR-TAS was performed using a femtosecond Ti:sapphire amplifier (wavelength: ≈800 nm and pulse width: <35 fs).[33] Pump and probe beams were generated using two TOPAS-Prime optical parametric amplifiers (from light conversion) for single kinetics measurements. To achieve both the same and opposite circularly polarized laser beams, quarter wave plates were utilized in the path of pump and probe beams. A white light continuum was generated by focusing an 800 nm laser beam on a CaF_2 crystal. The probe beam was detected under both conditions, with and without pump, using a mechanical chopper operating at a frequency of 500 Hz. A stepper motor was used to control the time delay between the pump and probe pulses *via* an optical delay line. Transient absorption (TA) spectra were recorded by dispersing the beam with a grating spectrograph (Acton Spectra Pro SP 2358), followed by a CCD array. Two photodiodes with variable gain were employed to record TA kinetics. Low-temperature measurements were conducted using a temperature controller from "Linkam Scientific Instruments" cooled with liquid nitrogen.

Computational details

All the electronic properties of MoS_2 with different substrates and individual monolayers were investigated using the Vienna *ab initio* Simulation Package (VASP), which is based on density functional theory.[34,35] The generalized gradient approximation in the Perdew, Burke, and Ernzerhof (PBE) form was adopted to describe the exchange–correlation function.[36] The projector-augmented wave method was used to treat the electron–ion interaction,[37] with the plane-wave cutoff energy set to 500 eV. The force and energy convergence criteria were set to 0.01 eV $Å^{-1}$ and 10^{-8} eV, respectively. A vacuum space larger than 50 Å was adopted to avoid adjacent layer interaction. The first Brillouin zone was sampled using Γ centered *k*-meshes of 5 × 5 × 1 and 3 × 3 × 1 for the supercell of MoS_2/sapphire and for the

supercell of MoS_2/quartz, respectively. The van der Waals (vdW) interaction was treated with DFT-D3 dispersion correction.[38] The Berry curvature was calculated using the VASPBERRY[39] code and the spin-polarized band structure was plotted using PYPROCAR.[40]

Results and discussion

Monolayer MoS_2 film

The optical image in Fig. 1(a) provides a visual representation of the CVD-grown MoS_2 on a sapphire substrate, illustrating a continuous layer covering a substantial area of the substrate surface. To further characterize the sample, its absorption and PL spectra were obtained, as depicted in Fig. 1(b). The absorption spectrum reveals two prominent peaks at approximately 1.85 eV and 2.01 eV, denoted as A and B, respectively, indicative of excitonic transitions associated with spin-split conduction and valence bands. Additionally, a higher energy absorption band at around 2.86 eV may be attributed to the band nesting effect. The PL spectrum, recorded at room temperature, reveals characteristic emission peaks. In accordance with previous findings in the literature, peaks observed at 1.85 eV and 1.96 eV were identified as the A and B excitons of monolayer MoS_2, respectively.[41–43] The sharp peaks appearing at ~ 1.78 eV in the PL spectra correspond to the Raman scattering feature of the sapphire substrate in good agreement with the previous reported literature.[44,45] These PL peaks provide valuable insights into the optical properties and excitonic behaviour of the monolayer MoS_2 film under investigation.

Furthermore, the thickness of MoS_2 was found to be 0.97 nm with the help of AFM by making a scratch on the film (Fig. S1), confirming the monolayer nature of the prepared sample. Although the intrinsic interlayer spacing in bulk MoS_2 is ~0.65–0.7 nm, AFM frequently measures monolayer MoS_2 at slightly higher apparent thicknesses due to factors like tip-sample convolution and substrate–layer interactions. Indeed, several studies report AFM-measured thicknesses of around 0.9 nm for monolayer MoS_2,[46–48] which encompasses our measured value of ~0.97 nm. Moreover, the monolayer nature

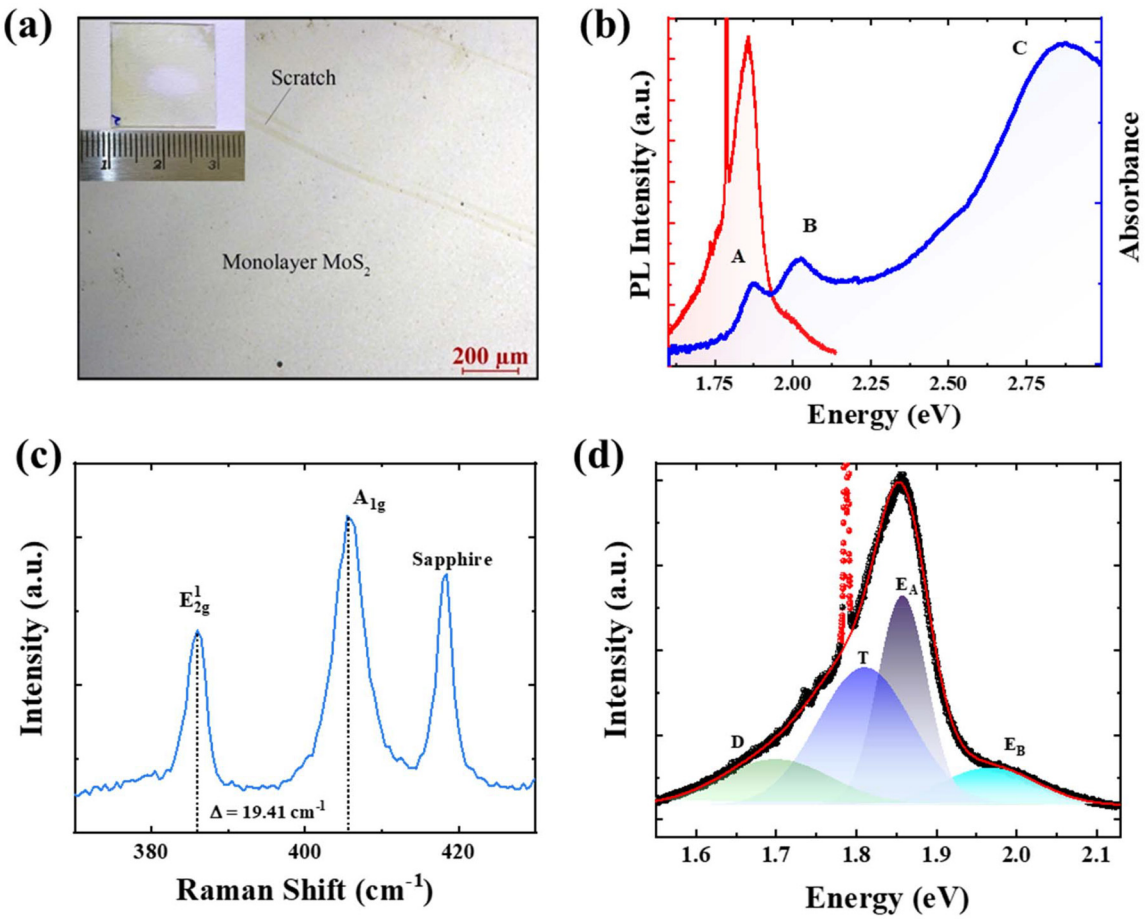

Fig. 1 (a) Optical image displaying large-area monolayer MoS_2 on a sapphire substrate grown using the CVD technique. (b) Absorption (blue curve) and PL (red curve) spectra of the sample. (c) Raman spectrum of monolayer MoS_2. (d) Fitting of the PL spectrum with the Gaussian function revealing four distinct peaks corresponding to B-excitons (E_B), A-excitons (E_A), charged excitons (T), and localized excitons (D).

of our samples is independently confirmed by Raman peak separation and pronounced PL emission, ensuring accurate layer identification. The Raman spectra of the MoS_2 film exhibit two distinct peaks, specifically the $E_{2g}{}^1$ and A_{1g} modes at ~385 cm^{-1} and ~404 cm^{-1}, respectively (Fig. 1(c)). These peaks correspond to the in-plane and out-of-plane vibrations of atoms within the monolayer. The difference between these two modes is ~19.4 cm^{-1}, which further supports the monolayer nature of the MoS_2 film, consistent with the literature available in several reports.[49–51] An additional Raman peak observed at around 419 cm^{-1} in Fig. 1(c) corresponds to the Raman signature of the underlying sapphire substrate.[52]

Subsequently, the PL spectrum was meticulously analyzed, with distinct excitonic features fitted using Gaussian peaks, as illustrated in Fig. 1(d). Notably, three prominent peaks were identified at 1.85 eV, 1.81 eV, and 1.69 eV, corresponding to the A-excitons, charged excitons (trions), and localized excitons respectively, and the peak at 2.01 eV corresponds to the B-exciton of monolayer MoS_2 based on the previously reported literature.[53–55] The full-width at half maximum (FWHM) values of these peaks were determined to be 61 meV (A-excitons), 117 meV (trions), and 139 meV (localized excitons), indicative of their respective line widths. Notably, the broader peak associated with localized excitons suggests the presence of significant defect states near the conduction band. Furthermore, the comparatively weaker emission intensity of trions compared to A-excitons implies a lower concentration of bright trions relative to excitons in the CVD-grown monolayer MoS_2 studied here.

Valley polarization in monolayer MoS_2

It is well known that monolayer TMDs have degenerate valleys as K and K′ corresponding to the opposite spin emerging from the broken inversion symmetry. For intervalley scattering or depolarization, spin–flip of excited electrons is required. Intravalley scattering is energetically forbidden as the spin splitting in monolayer MoS_2 is very large (~0.146 eV) at the K point.[56,57] The DOP is defined as:[7]

$$\delta = \frac{N_{A(K)} - N_{A(K')}}{N_{A(K)} + N_{A(K')}} \quad (1)$$

where $N_{A(K)}$ and $N_{A(K')}$ are the population of charge carriers in the K and K′ valleys, respectively. Following photoexcitation of the K valley by a right circularly polarized (σ^+) pump pulse, we can monitor the exciton population dynamics in the pumped (K) and unpumped (K′) valleys with the help of the same circularly polarized (SCP) and opposite circularly polarized (OCP) probes, respectively. In this case, the HR-TA signal at a valley is proportional to the exciton population, $N_{A(K)}(N_{A(K')})$ of the corresponding valley, K(K′). Therefore, the DOP can be estimated from the following relationship:

$$\delta = \frac{\Delta A_{SCP} - \Delta A_{OCP}}{\Delta A_{SCP} + \Delta A_{OCP}} \quad (2)$$

The time evolution of the difference between the two HR-TA kinetics (*i.e.*, $|\Delta A_{SCP} - \Delta A_{OCP}|$) reflects the dynamics of valley depolarization. Furthermore, the DOP can be expressed as:[58]

$$\delta = \frac{\delta_0(1-\rho)^2}{1 + \frac{2\tau_0}{\tau_v}} \quad (3)$$

where δ_0 is the theoretical DOP, τ_0 represents the exciton lifetime, and τ_v corresponds to the intervalley scattering lifetime. The factor $(1 - \rho)$ refers to selectivity in the initial excitation and $\delta_0(1 - \rho)^2$ represents the initial valley polarization. The parameter ρ accounts for the influence of impurities, defects, phonons, and substrate-induced recombination processes, all of which contribute to intervalley mixing *via* momentum scattering, with $0 < \rho < 1$. Experimentally observed DOP values lower than unity are ascribed to inevitable intervalley scattering processes. Previous studies have suggested that valley depolarization is controlled by the MSS mechanism, wherein the exchange interaction between electrons and holes across different valleys facilitates intervalley exciton transitions.[22,59,60] This transition involves the virtual recombination of an exciton in the K valley and its subsequent generation in the K′ valley.

To investigate the valley polarization and its depolarization dynamics, we performed HR-TAS on large-area monolayer MoS_2. As reported in the literature, valley polarization is strongly dependent on the excitation energy and tends to decrease with increasing excitation energy.[61,62] For HR decay kinetics measurements, we employed coherent pump and probe pulses with photon energies corresponding to the A-excitonic bleach position. The energetic positions of the A-excitonic bleach for the studied samples were determined from our recent work, in which we explored the charge carrier dynamics of monolayer MoS_2 on various substrates.[32]

Fig. 2(a) and (b) show the decay kinetics of A-excitons in the MoS_2 films grown on sapphire measured using the same (SCP, black curve) and opposite (OCP, red curve) circularly polarized pump and probe pulses. The difference between these signals, $|\Delta A_{SCP} - \Delta A_{OCP}|$, is plotted as a function of delay time (blue dots) in the same figures, representing the valley depolarization dynamics. The maximum DOP (δ_m) and depolarization time (τ_d) are found to be 23% and 0.5 ps, respectively, at room temperature. Notably, δ_m increases to 31% at a lower temperature (77 K), aligning well with previous studies;[17,62] the depolarization time also increases to 2.5 ps at 77 K. This trend can be attributed to the expected increase in the momentum-dependent effective magnetic field, $\Omega(p)$, with the temperature, owing to intensified exchange interactions. Consequently, spin precession and decoherence accelerate, leading to a reduction in the exciton intervalley scattering time and less valley polarization at room temperature. Theoretical insights suggest that the long-range exchange interaction behaves like a momentum-dependent effective magnetic field ($\Omega(p)$), with p as the center-of-mass momentum of the A-excitons.[22] Analogous to the DP mechanism, exciton spins

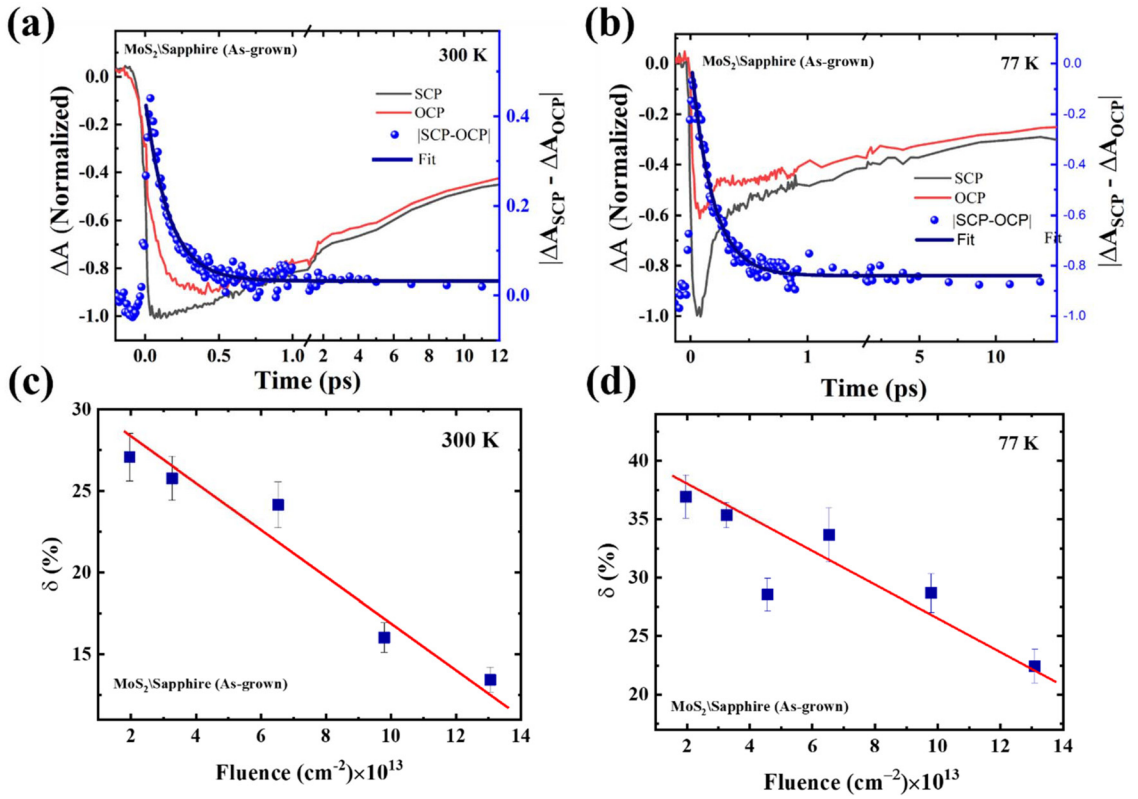

Fig. 2 Helicity-resolved TA kinetics of the A-excitons in the as-grown sample measured using pump and probe energies of (a) 1.85 eV at 300 K and (b) 1.89 eV at 77 K. The TA kinetics were normalized to the maximum of the ΔA_{SCP} signal. The valley depolarization dynamics, obtained by subtracting the signals ΔA_{SCP} and ΔA_{OCP}, is represented by the blue dots. The maximum DOP plotted as a function of injected exciton density at (c) 300 K and (d) 77 K (the red lines indicate the decreasing trend of DOP with fluence).

with different momentums precess around this effective magnetic field at varying frequencies, resulting in a free-induction decay akin to spin relaxation caused by inhomogeneous broadening from randomly oriented effective SOC fields. The precession frequency, attributable to the momentum-dependent effective magnetic field induced by the long-range exchange interaction between exciton spin states, is expressed as $\omega(p) \approx \sqrt{5}C\mu(1)|p|/h$, where $\mu(1)$ and C are material-specific parameters. Similarly, in analogy to the DP mechanism, exciton momentum scattering mitigates inhomogeneous broadening in the strong scattering regime, as delineated by the relationship:

$$\tau_{s(v)}{}^{-1} = \Omega^2(p)\tau_p^* \quad (4)$$

where $\tau_{s(v)}$ represents the spin relaxation time and τ_p^* signifies the momentum relaxation time of excitons *via* scattering.

To study the influence of excitation density on the valley polarization, a broad range of pump fluences was employed to systematically vary the exciton density. Valley polarization was initially evaluated at room temperature by recording HR-TA kinetics at various excitation fluences (Fig. S2). The value of δ_m decreases with increasing exciton density in monolayer MoS_2 as-grown on sapphire (Fig. 2(c)). This trend suggests that valley depolarization is predominantly governed by the MSS mechanism driven by intervalley electron–hole exchange interactions. As the exciton density increases, the Coulomb exchange interaction strengthens, leading to coherent mixing of valley states (K and K′) and resulting in valley depolarization. Subsequently, the same set of HR-TA measurements was repeated at 77 K (Fig. S2). A comparable trend in the variation of δ_m with the exciton density is observed (Fig. 2(d)). The persistence of this behavior at low temperatures indicates that thermal effects are not the primary driver of depolarization. Instead, intrinsic mechanisms such as exciton–exciton interactions and exciton–phonon scattering are likely contributors. At higher excitation fluence, enhanced exciton–exciton interactions lead to increased intervalley scattering, while exciton–phonon interactions further assist in reducing valley polarization. Since the DP mechanism primarily affects free carriers and is less relevant for exciton-driven valley depolarization in MoS_2, the MSS mechanism remains the most plausible explanation for the observed dependence of valley polarization on exciton density.

Substrate-induced modulation of valley polarization

It is evident from eqn (3) that the DOP strongly depends on the values of ρ, which represents defect/impurity and substrate-related or phonon-assisted recombination that leads to intervalley scattering. Hence, the DOP could be affected by the

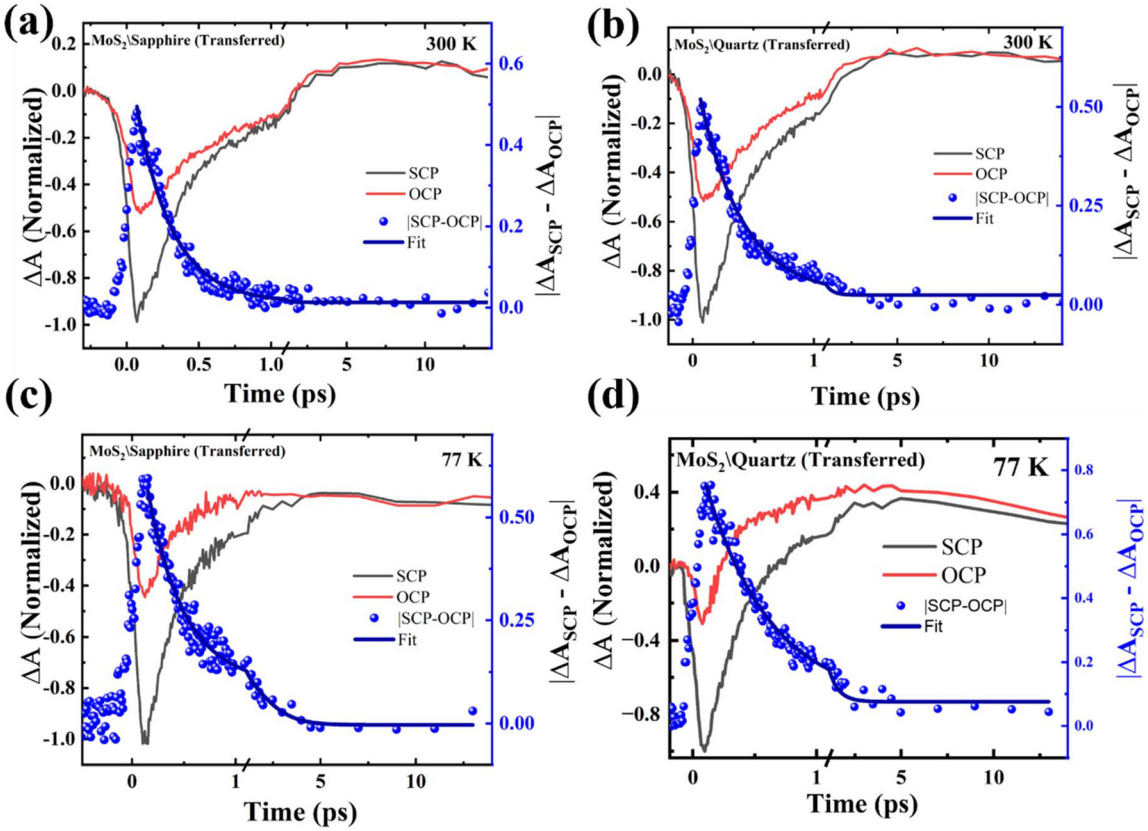

Fig. 3 HR-TA kinetics for large-area monolayer MoS_2 transferred on sapphire (a and c) and quartz (b and d) substrates measured at 300 K and 70 K, respectively. TA kinetics were recorded using an SCP- and OCS-polarized pump and a probe with coherent excitation (~1.85 eV at 300 K and 1.89 eV at 77 K). The quantity $|\Delta A_{SCP} - \Delta A_{OCP}|$ (represented by the right-side ordinate) was plotted as a function of time (blue dotted curves) for each case.

Table 1 Maximum DOP and depolarization time of the as-grown and transferred monolayer MoS_2 at different temperatures

	300 K		77 K	
Sample	δ_m (%)	τ_d (ps)	δ_m (%)	τ_d (ps)
MoS_2\sapphire (as-grown)	23	0.51 ± 0.04	31	2.58 ± 0.06
MoS_2\sapphire (transferred)	32	0.83 ± 0.10	42	4.5 ± 0.07
MoS_2\quartz (transferred)	33	1.8 ± 0.11	57	5.8 ± 0.14

substrate change. To explore this, we conducted HR-TA kinetics measurements of the transferred monolayer MoS_2 on sapphire and quartz at two different temperatures as depicted in Fig. 3. We estimated the values of δ_m and τ_d for each sample and they are given in Table 1. Both the DOP and depolarisation time are found to be enhanced in the transferred samples as compared to the as-grown sample irrespective of temperature (Table 1).

Furthermore, we measured the excitation fluence-dependent HR-TA kinetics of the transferred samples at 300 K and 77 K on sapphire (Fig. S3) and quartz (Fig. S4) substrates. The analysis of excitation fluence-dependent DOP of transferred samples (Fig. S5) revealed a similar trend of decreasing valley polarization with increasing exciton density, reinforcing the role of the MSS mechanism in both the as-grown and transferred samples.

To understand the reason behind the increase of the DOP and depolarization time in transferred MoS_2 on sapphire and quartz, we analysed their absorption and emission properties. Fig. S6(a) and (b) show a comparison of the absorption and PL spectra of the as-grown and transferred samples, respectively. Notably, we observed distinct changes in the PL spectra of the transferred samples, including a broadening and red shift compared to the pristine monolayer on sapphire. These observations are in good agreement with our previous work where we have shown the strain-induced effects that alter dielectric environments upon transfer.[32] Our fitting analysis of PL spectra further reveals a slight red shift in the trionic peak and an increased contribution to the emission spectra, consistent with previous studies linking trionic emission to induced strain. Harats *et al.*[29] demonstrated that the trionic emission is proportional to the induced strain caused by the funnelling effect, and the red shift in the trionic peak also agrees well with the results. Additionally, the presence of defect states is more prominent on the quartz substrate, as evidenced by the higher defect peak intensity in the PL spectrum. Furthermore, we conducted TAS studies of our samples at 300 K and 77 K, as shown in Fig. S6(c) and (d), respectively. At the low temperature, the

TAS of monolayer MoS_2 exhibits shifts in the A and B excitonic bleach signals, along with reduced broadening and a longer decay time of these features. These observations can be attributed to the interplay of several factors. First, at lower temperatures, thermal energy is minimized, leading to decreased exciton–phonon coupling and phonon-induced relaxation processes. As a result, excitons experience less scattering by lattice vibrations, leading to longer exciton lifetimes and narrower spectral line widths. Additionally, the reduction in thermal energy alters the population distribution of excitonic states, causing shifts in the peak positions of the A and B excitonic features. The TA spectra of the transferred monolayer MoS_2 on sapphire and quartz substrates are shown in Fig. S6(e and f). One can observe the increased broadening in the bleach spectra of transferred samples, which could be due to the increased interfacial defects during the transferred process. Notably, a slight red shift is also observed in the transferred sample, which supports the induced strain as we have found in the PL analysis. The observations from PL and TAS analyses highlight the intricate interplay between substrate-induced strain and defect formation, influencing the band structure and binding energy of excitons, thus influencing the optical properties of transferred monolayer MoS_2. Furthermore, AFM mapping of the transferred samples reveals ripple formation and surface height variations, providing direct evidence of transfer-induced strain fields in monolayer MoS_2 (Fig. S1(c and d)). The substrate-induced strain and interfacial defects could alter valley polarisation and dynamics, as we have seen in the case of transferred MoS_2 (Table 1). This complex interplay between strain, exciton binding energy, and valley polarization highlights the necessity of carefully selecting substrates for tailored optoelectronic properties.

It is important to note that intervalley scattering can play dual roles in determining valley polarization. Under certain conditions, asymmetric intervalley scattering pathways can generate or even enhance valley polarization, as demonstrated recently.[63] However, in our transferred MoS_2 samples, the dominant effect arises from the suppression of depolarizing intervalley scattering channels, particularly those governed by the MSS mechanism. The MSS mechanism, originating from electron–hole exchange interactions between the K and K′ valleys, leads to efficient valley depolarization. In contrast, the strain fluctuations and varying defect densities in transferred MoS_2 minimize these depolarization channels, thereby prolonging the valley polarization lifetime. Thus, while scattering-assisted polarization generation is possible in specific regimes, our experimental observations are primarily governed by the suppression of depolarization pathways, which explains the enhanced valley polarization in the transferred samples.

The increase in trion-related PL intensity shown in Fig. S6(b) after the transfer indicates enhanced trion formation, which may influence valley dynamics. Trions are known to exhibit longer valley depolarization times than neutral excitons due to their reduced electron–hole exchange interaction.[64–66] Although our transient absorption analysis is dominated by excitonic resonances and the extracted depolarization times primarily reflect neutral exciton dynamics, trion-related processes may indirectly contribute to sustaining valley polarization.

By bridging the insights from valley depolarization and optical absorption/emission characteristics, our results provide a comprehensive understanding of the substrate-dependent modifications in monolayer MoS_2. The achieved control over valley polarization with substrate engineering in monolayer TMDs could be useful for the development of next-generation information and photonic devices. For instance, Pu *et al.*[67] realized a room-temperature chiral LED in WSe_2 and WS_2 on a plastic substrate *via* introducing biaxial strain. Nonetheless, we have seen that the valley polarization can survive up to high temperatures after introducing strain on the monolayer TMDs, thus it can play a vital role in room-temperature valleytronic devices. Furthermore, excitonic valley coherence[60] and optoelectronic devices and systems based on the manipulation of the electrons' valley index have been demonstrated.[68–70] Therefore, the achieved control over valleytronic properties of layered MoS_2 could significantly enhance the potential of monolayer TMDs for next-generation optoelectronic applications.

Theoretical calculations

To gain deeper insight into the origin of the enhanced valley polarization in the transferred MoS_2 monolayer, we performed first-principles calculations based on density functional theory (DFT). The top and side views of the optimized geometry of the MoS_2 unit cell, as well as the MoS_2/sapphire and MoS_2/quartz heterostructures, are shown in SI Fig. S7. The elastic constant and phonon calculations confirm the mechanical and thermodynamic stability of the structure. Fig. 4(a) depicts the z-component of the spin (S_z)-projected band structure of the MoS_2 unit cell calculated using the PBE+SOC method. The band gaps at the K and K′ points are equal (E_g (K/K′) = 1.61 eV), confirming the preservation of spin–valley characteristics. The spin splitting at the valence band maximum (VBM) at K/K′ is observed to be Δv = 147.5 meV, while the conduction band minimum (CBM) exhibits a negligible spin splitting of Δc = 2.9 meV. The spin contrast is evident from the colour mapping (Fig. 4(a)), where the opposite spin states at K and K′ reaffirm the spin–valley locking, a key feature for valleytronic applications.

Beyond the spin–valley locking observed in the band structure, the Berry curvature, $\Omega_n^z(\mathrm{K})$, and orbital magnetic moment, $m(\mathrm{K})$, are the two essential quantities in valleytronics.[71] The Berry curvature, in particular, plays a crucial role in the electronic transport properties of the material and can be computed using the Kubo formula:[72–74]

$$\Omega_n^z(\mathrm{K}) = -2\mathrm{Im}\sum_{m\neq n}\frac{\langle\psi_{n\mathrm{K}}|\hat{v}_x|\psi_{m\mathrm{K}}\rangle\langle\psi_{m\mathrm{K}}|\hat{v}_y|\psi_{n\mathrm{K}}\rangle}{(E_{n\mathrm{K}}-E_{m\mathrm{K}})^2} \quad (5)$$

where $\hat{v}_{x,y}$ are the velocity operators. Here, the summation is over the occupied states and plotted along a high-symmetry

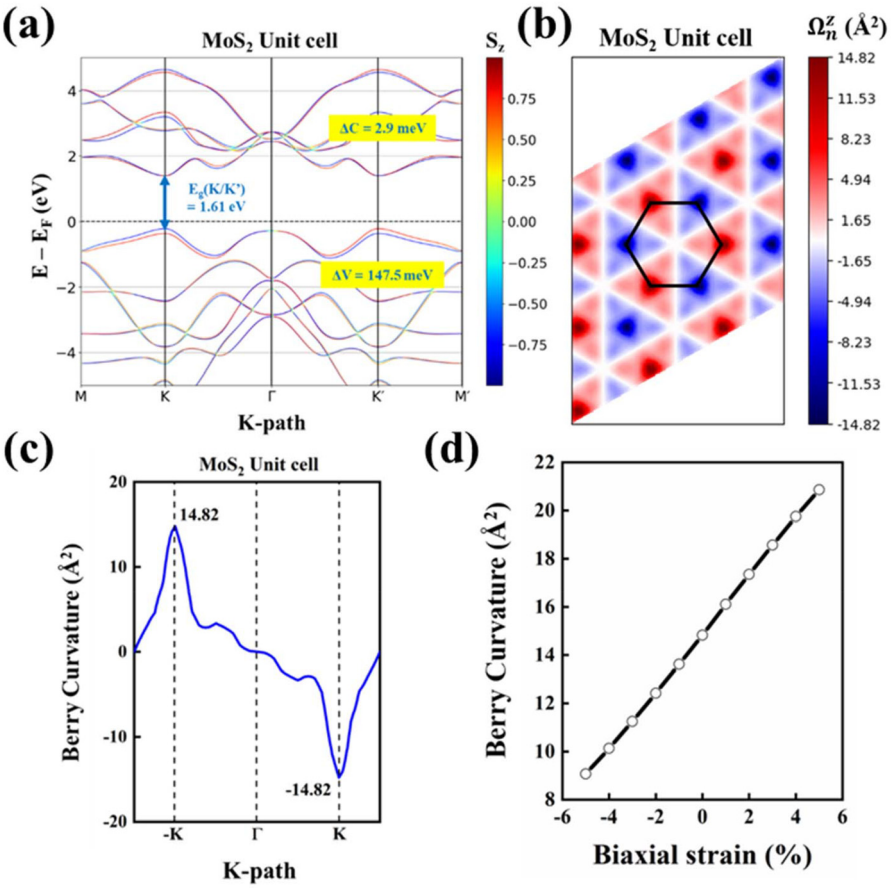

Fig. 4 (a) The S_z (z-component of spin)-projected band structure of the MoS_2 unit cell considering the SOC effect. The Berry curvature (b) as a 2D plot and (c) as a line along the K points in the first BZ of the MoS_2 unit cell. (d) Variation of Berry curvature in the MoS_2 unit cell with applied biaxial strain.

K-path. The $k{\cdot}p$ Hamiltonian, including SOC, near K/K′ at the band edges is given by:

$$H = at(\tau_z K_x \sigma_x + K_y \sigma_y) + \frac{\Delta}{2}\sigma_z - \lambda\tau\frac{\sigma_z - 1}{2}S_z \qquad (6)$$

where a is the lattice spacing, t denotes the nearest-neighbour hopping integral, and τ_z (= ±1) is the valley index. The parameters $\sigma_{x/y/z}$, λ, Δ, and S_z represent the Pauli matrix ranged by the valence and conduction states, the spin splitting, the band gap, and the Pauli matrix for spin, respectively.

Fig. 4(b) presents the 2D distribution of the Berry curvature for the MoS_2 unit cell, while Fig. 4(c) shows its variation along the high-symmetry K-path in the first Brillouin zone (BZ). The magnitude of the Berry curvature is equal with an opposite sign at the K and K′ points, consistent with the spin-splitting characteristics observed in the spin-projected band structure. This confirms that valley polarization can be induced in monolayer MoS_2 through optical selective excitation, highlighting its intrinsic valleytronic properties. Moreover, the Berry curvature with increasing strain was computed and is presented in Fig. 4(d). The results reveal that valley polarization is enhanced with increasing strain, indicating a strain-driven modulation of the Berry curvature. This trend aligns with our experimental findings, as shown in Table 1, where the transferred MoS_2 sample exhibits a higher valley polarization compared to the as-grown sample.

Furthermore, the Berry curvature of the MoS_2/sapphire and MoS_2/quartz heterostructures was computed to understand the substrate-induced modifications. Fig. 5(a) presents the z-component of the spin-projected band structure for the MoS_2/sapphire heterostructure, revealing how substrate interactions modify the electronic states while preserving key valley-dependent properties. Notably, the VB edge is primarily contributed by the sapphire substrate, while the CB edge remains dominated by MoS_2, indicating a charge transfer effect that further influences the band alignment and valley-dependent electronic properties. Despite the introduction of substrate-induced perturbations, the spin splitting at the K and K′ points remains intact, confirming the robustness of SOC in MoS_2. The reduction in conduction band splitting Δc from 70.4 meV to 2.9 meV and the significant enhancement of Δv from 17.4 meV to 147.5 meV highlight the substrate's asymmetric influence on spin–valley interactions. The expansion to a three-unit MoS_2 supercell (Fig. S7) introduces band folding,

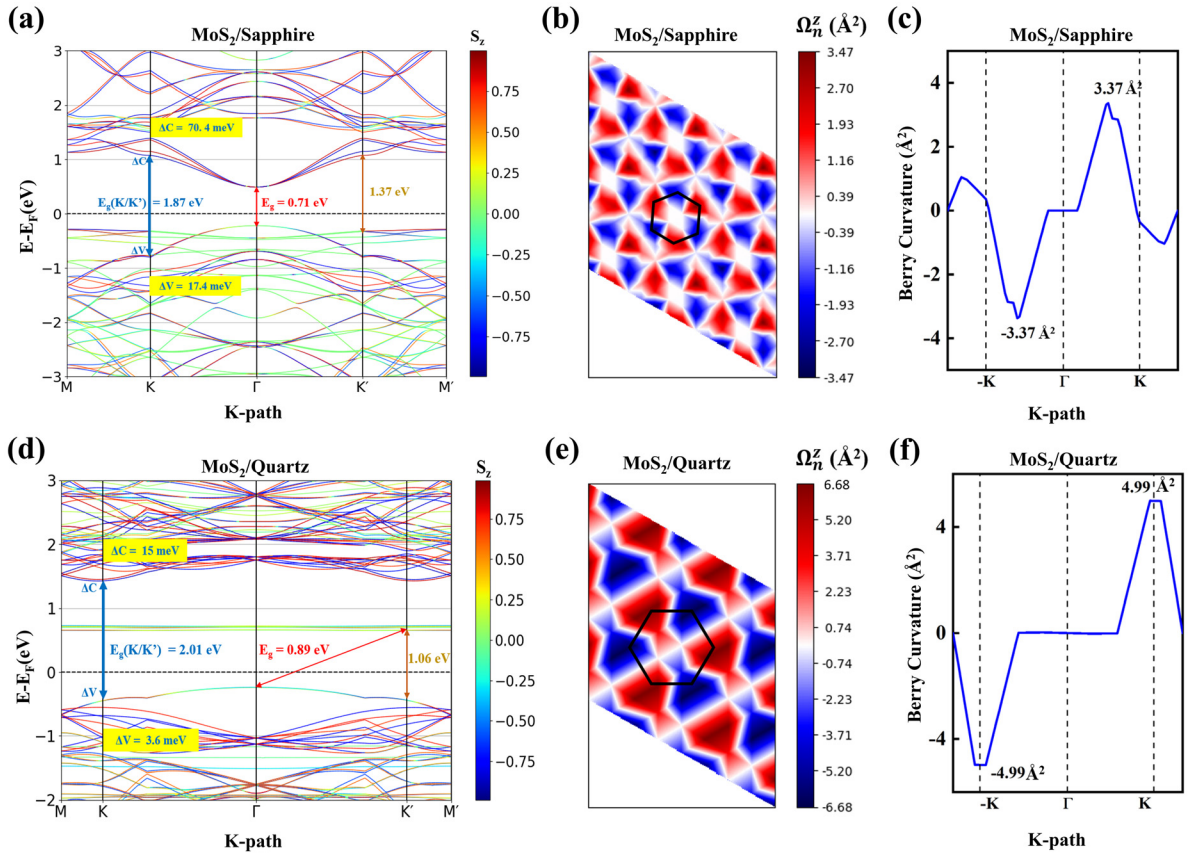

Fig. 5 (a) The S_z-projected band structure of MoS_2 on a sapphire substrate considering the SOC effect. The Berry curvature (b) as a 2D plot and (c) as a line along K points in the first BZ. (d) The S_z-projected band structure of MoS_2 on a quartz substrate considering the SOC effect. The Berry curvature (e) as a 2D plot and (f) as a line along the K points in the first BZ.

leading to a denser band dispersion while maintaining the core valley characteristics. This confirms that the essential physics of MoS_2, particularly the Berry curvature and valley-selective properties, remains preserved even in a supercell framework. Additionally, a comparison with the pristine MoS_2 band structure (Fig. S8) reveals that the observed spectral complexity arises not only from substrate interactions but also from the intrinsic multi-band nature of MoS_2 in an extended real-space periodicity. The presence of a reduced fundamental band gap at Γ (0.71 eV), along with a valley-specific band gap at K/K′ (1.87 eV), suggests that hybridization effects in MoS_2/sapphire play a crucial role in reshaping the band structure, potentially enhancing valley polarization. These findings establish MoS_2/sapphire as a promising platform for valleytronic and spintronic applications, where controlled valley splitting in the valence band can be leveraged for optoelectronic and transport phenomena.

Fig. 5(b and c) illustrate the Berry curvature of MoS_2/sapphire along high-symmetry K-points. Compared to the free-standing monolayer MoS_2, the valley polarization in the presence of a sapphire substrate remains nearly unchanged, as indicated by the negligible reduction in the maximum Berry curvature value from 3.38 Å^2 to 3.37 Å^2. This suggests that the substrate does not significantly alter the intrinsic Berry curvature-driven valley properties of MoS_2. However, in the supercell calculations, the Berry curvature magnitude is noticeably reduced compared to the unit cell for MoS_2, emphasizing the influence of band folding and extended periodicity on its distribution.

In the case of the quartz substrate, to avoid the lattice mismatch, we constructed a heterostructure with a bigger supercell containing 7 units of MoS_2. The top and side views of the optimized geometry of the MoS_2 monolayer on the quartz substrate are shown in Fig. S7. The mechanical and thermodynamic stability of the structure was confirmed by elastic constant and phonon calculations. Fig. 5(d) presents the z-component of the spin-projected band structure for MoS_2/quartz, revealing the substrate-induced modifications in electronic states. Unlike MoS_2/sapphire, the conduction band is primarily contributed by quartz, while the valence band originates from MoS_2, resulting in a type-II band alignment.

While the bandgap at K/K′ remains 2.01 eV, the fundamental gap reduces to 0.89 eV, indicating strong interlayer interactions. Additionally, the direct bandgap relative to the CB from quartz is 1.06 eV, which plays a crucial role in enhancing valley polarization through interfacial coupling. The splitting

at the valence (3.6 meV) and conduction bands (15 meV) further emphasizes the influence of quartz in modifying the electronic structure while preserving the intrinsic spin–orbit interactions of MoS_2. Fig. 5(e) and (f) demonstrate that the Berry curvature in the MoS_2/quartz heterostructure remains comparable to that of pristine MoS_2 but exhibits a slight reduction in magnitude at the K and K′ points. This indicates that quartz perturbs the electronic environment more significantly than sapphire, leading to noticeable modifications in the Berry curvature distribution. Despite this, the intrinsic valleytronic properties of MoS_2 are largely preserved.

We further corroborate the differences in valley polarization in monolayer MoS_2 on sapphire and quartz substrates through transition dipole moment (TDM) calculations. The TDM provides insight into the probability of specific electronic transitions and serves as a key indicator of how substrate-induced effects influence optical selection rules and valley-specific absorption in the material. In quantum mechanics, the transition probability from one eigenstate Ψ_1 to another eigenstate Ψ_1 is given by $\left|\vec{M}_{21}\right|^2$, and $\vec{M}_{21}$ is called the TDM for this transition. In mathematical form, it can be written as[75]

$$\vec{M}_{21} = \int \Psi_1 \vec{\mu} \Psi_2 \mathrm{d}\tau \tag{7}$$

where $\vec{\mu}$ is the dipole moment operator.

A schematic representation of the MoS_2 energy levels in the MoS_2/sapphire and MoS_2/quartz heterostructures is depicted in Fig. S9(a) and (b), respectively, with the corresponding TDMs tabulated in Table 2. The MoS_2 unit cell exhibits a transition dipole moment squared (TDM^2) difference of 21.29%. When considering transitions at the K and K′ bands originating from MoS_2, independent of the band edges, a TDM^2 difference of 39.18% is observed for the MoS_2/sapphire heterostructure. However, transitions from the sapphire states to MoS_2 at the K/K′ points contribute a much lower TDM^2 difference of 19.18%. Notably, the actual TDM^2 values in the heterostructures are significantly reduced compared to the pristine MoS_2 unit cell.

In both MoS_2/quartz and MoS_2/sapphire heterostructures, the valley-contrasting SOC splitting at the K and K′ points is preserved, maintaining time-reversal symmetry. However, a crucial difference emerges in TDM^2; while both heterostructures exhibit a disparity between spin-up and spin-down TDM^2, the MoS_2/quartz system exhibits a significantly larger difference (58.1%). According to optical selection rules, interband transitions are allowed only between states with the same spin, meaning that circularly polarized light selectively excites carriers in a spin-dependent manner. As a result, even in the absence of any difference in the bandgap at K and K′, valley polarization arises due to differential absorption between the spin-up and spin-down states. The larger disparity in TDM^2 for MoS_2/quartz leads to a more pronounced difference in absorption for right- and left-circularly polarized light, thereby enhancing valley polarization compared to MoS_2/sapphire. This finding underscores the crucial role of spin-dependent optical matrix elements in controlling valley polarization, independent of energy level asymmetry at the K and K′ points. This theoretical insight aligns with experimental observations, where the MoS_2/quartz (transferred) heterostructure exhibits a significantly higher valley polarization compared to MoS_2/sapphire (transferred), highlighting the crucial role of spin-dependent transition dipole moments in enhancing valley-selective optical responses.

Table 2 Transition dipole moment calculated for MoS_2, MoS_2/sapphire and MoS_2/quartz

Transition	TDM^2 (up)	TDM^2 (down)	Diff. TDM^2 (%)
MoS_2 unit cell			
25/26 to 27/28	314.91	381.98	21.29
MoS_2/sapphire			
163/164 to 175/176	0.000656	0.00109	39.81
173/174 to 175/176	0.01178	0.0952	19.18
MoS_2/quartz			
325/326 to 333/334	0.00043	0.00018	58.1
325/326 to 327/328	0.3216	0.38433	19.18

Conclusions

In summary, here, we provide a combined experimental and theoretical investigation into valley polarization enhancement in transferred monolayer MoS_2, revealing the critical roles of substrate-induced strain, defect states, and transition dipole moment modulation. Using helicity-resolved transient absorption spectroscopy, we demonstrate that transferred MoS_2 exhibits significantly higher valley polarization and longer depolarization times compared to the as-grown samples, particularly under reduced excitation fluence and cryogenic conditions. This enhancement is attributed to suppressed intervalley scattering *via* the Maialle–Silva–Sham mechanism and strain-driven modification of the spin-dependent transition dipole moments—validated through first-principles calculations of Berry curvature and optical selection rules. The observation of fluence-dependent depolarization and temperature-invariant trends underscores the robustness of substrate-induced valley control. The enhanced valley polarization and extended valley lifetime observed in transferred MoS_2 highlight the effectiveness of strain, defect engineering, and spin-dependent transition dipole moments in tuning valley dynamics. Our finding suggests that strain-, defect-, and substrate-engineered monolayer TMDs can transition from fundamental valley physics to practical valleytronic devices, such as strain-modulated photodetectors, valley-based emitters, and flexible valleytronic circuits.

Conflicts of interest

There are no conflicts to declare.

Data availability

The data are available upon reasonable request from the corresponding author.

Supplementary Information includes pump fluence estimation, helicity-resolved TA data, optical and AFM characterizations, and DFT-based band structure and Berry curvature analyses of MoS_2 on sapphire and quartz, supporting the substrate-induced valley polarization discussed in the main text. See DOI: https://doi.org/10.1039/d5nr02938d.

Acknowledgements

A. S. and S. K. P. express their appreciation for the financial assistance provided by the Science and Engineering Research Board (SERB), Government of India (Grant No. CRG/2018/003045). F. I. S. and A. D. S. would like to acknowledge the supercomputing facilities provided by INST, Mohali (in-house) and PARAM Smriti at NABI, Mohali, under the National Supercomputing Mission, Government of India. All the authors extend their gratitude to the Advanced Materials Research Centre (AMRC) at IIT Mandi for granting access to experimental facilities. The authors also acknowledge the use of ChatGPT for improving the language quality of the manuscript.

References

1 F. Sattari and S. Mirershadi, Spin and valley dependent transport in a monolayer MoS_2 superlattice with extrinsic Rashba spin–orbit interaction, *J. Magn. Magn. Mater.*, 2020, **514**, 167256.
2 R. Suzuki, M. Sakano, Y. J. Zhang, R. Akashi, D. Morikawa, A. Harasawa, K. Yaji, K. Kuroda, K. Miyamoto, T. Okuda, *et al.*, Valley-dependent spin polarization in bulk MoS_2 with broken inversion symmetry, *Nat. Nanotechnol.*, 2014, **9**(8), 611–617.
3 D. Xiao, G.-B. Liu, W. Feng, X. Xu and W. Yao, Coupled spin and valley physics in monolayers of MoS_2 and other group-VI dichalcogenides, *Phys. Rev. Lett.*, 2012, **108**(19), 196802.
4 K. F. Mak, K. L. McGill, J. Park and P. L. McEuen, The valley Hall effect in MoS_2 transistors, *Science*, 2014, **344**(6191), 1489–1492.
5 X. Xu, W. Yao, D. Xiao and T. F. Heinz, Spin and pseudospins in layered transition metal dichalcogenides, *Nat. Phys.*, 2014, **10**(5), 343–350.
6 H. Zeng, J. Dai, W. Yao, D. Xiao and X. Cui, Valley polarization in MoS_2 monolayers by optical pumping, *Nat. Nanotechnol.*, 2012, **7**(8), 490–493.
7 K. F. Mak, K. He, J. Shan and T. F. Heinz, Control of valley polarization in monolayer MoS_2 by optical helicity, *Nat. Nanotechnol.*, 2012, **7**(8), 494–498.
8 A. Soni and S. K. Pal, Valley degree of freedom in two-dimensional van der Waals materials, *J. Phys. D: Appl. Phys.*, 2022, **55**(30), 303003.
9 T. LaMountain, J. Nelson, E. J. Lenferink, S. H. Amsterdam, A. A. Murthy, H. Zeng, T. J. Marks, V. P. Dravid, M. C. Hersam and N. P. Stern, Valley-selective optical Stark effect of exciton-polaritons in a monolayer semiconductor, *Nat. Commun.*, 2021, **12**(1), 4530.
10 L. Ju, L. Wang, X. Li, S. Moon, M. Ozerov, Z. Lu, T. Taniguchi, K. Watanabe, E. Mueller, F. Zhang, *et al.*, Unconventional valley-dependent optical selection rules and landau level mixing in bilayer graphene, *Nat. Commun.*, 2020, **11**(1), 2941.
11 T. Roy, M. Tosun, J. S. Kang, A. B. Sachid, S. B. Desai, M. Hettick, C. C. Hu and A. Javey, Field-effect transistors built from all two-dimensional material components, *ACS Nano*, 2014, **8**(6), 6259–6264.
12 T. Akama, W. Okita, R. Nagai, C. Li, T. Kaneko and T. Kato, Schottky solar cell using few-layered transition metal dichalcogenides toward large-scale fabrication of semitransparent and flexible power generator, *Sci. Rep.*, 2017, **7**(1), 11967.
13 A. Hasani, Q. V. Le, M. Tekalgne, M.-J. Choi, T. H. Lee, H. W. Jang and S. Y. Kim, Direct synthesis of two-dimensional MoS_2 on p-type Si and application to solar hydrogen production, *NPG Asia Mater.*, 2019, **11**(1), 47.
14 A. Soni, D. Kushavah, L.-S. Lu, W.-H. Chang and S. K. Pal, Efficient multiple exciton generation in monolayer MoS_2, *J. Phys. Chem. Lett.*, 2023, **14**(12), 2965–2972.
15 M. S. Choi, D. Qu, D. Lee, X. Liu, K. Watanabe, T. Taniguchi and W. J. Yoo, Lateral MoS_2 p–n Junction formed by chemical doping for use in high-performance optoelectronics, *ACS Nano*, 2014, **8**(9), 9332–9340.
16 J. Ahn, P. J. Jeon, S. R. A. Raza, A. Pezeshki, S.-W. Min, D. K. Hwang and S. Im, Transition metal dichalcogenide heterojunction PN diode toward ultimate photovoltaic benefits, *2D Mater.*, 2016, **3**(4), 045011.
17 C. R. Zhu, K. Zhang, M. Glazov, B. Urbaszek, T. Amand, Z. W. Ji, B. L. Liu and X. Marie, Exciton valley dynamics probed by Kerr rotation in WSe_2 monolayers, *Phys. Rev. B: Condens. Matter Mater. Phys.*, 2014, **90**(16), 161302.
18 S. Dal Conte, F. Bottegoni, E. A. A. Pogna, D. De Fazio, S. Ambrogio, I. Bargigia, C. D'Andrea, A. Lombardo, M. Bruna, F. Ciccacci, *et al.*, Ultrafast valley relaxation dynamics in monolayer MoS_2 probed by nonequilibrium optical techniques, *Phys. Rev. B:Condens. Matter Mater. Phys.*, 2015, **92**(23), 235425.
19 X. Song, S. Xie, K. Kang, J. Park and V. Sih, Long-lived hole spin/valley polarization probed by Kerr rotation in monolayer WSe_2, *Nano Lett.*, 2016, **16**(8), 5010–5014.
20 M. M. Glazov, T. Amand, X. Marie, D. Lagarde, L. Bouet and B. Urbaszek, Exciton fine structure and spin decoherence in monolayers of transition metal dichalcogenides, *Phys. Rev. B:Condens. Matter Mater. Phys.*, 2014, **89**(20), 201302.

21 L. Wang and M. W. Wu, Intrinsic electron spin relaxation due to the D'yakonov–Perel' mechanism in monolayer MoS_2, *Phys. Lett. A*, 2014, **378**(18), 1336–1340.
22 T. Yu and M. W. Wu, Valley depolarization due to intervalley and intravalley electron–hole exchange interactions in monolayer MoS_2, *Phys. Rev. B:Condens. Matter Mater. Phys.*, 2014, **89**(20), 205303.
23 W. H. Chae, J. D. Cain, E. D. Hanson, A. A. Murthy and V. P. Dravid, Substrate-induced strain and charge doping in CVD-grown monolayer MoS_2, *Appl. Phys. Lett.*, 2017, **111**(14), 143106.
24 D. Domaretskiy, M. Philippi, M. Gibertini, N. Ubrig, I. Gutiérrez-Lezama and A. F. Morpurgo, Quenching the bandgap of two-dimensional semiconductors with a perpendicular electric field, *Nat. Nanotechnol.*, 2022, **17**(10), 1078–1083.
25 K. Wang, K. De Greve, L. A. Jauregui, A. Sushko, A. High, Y. Zhou, G. Scuri, T. Taniguchi, K. Watanabe, M. D. Lukin, *et al.*, Electrical control of charged carriers and excitons in atomically thin materials, *Nat. Nanotechnol.*, 2018, **13**(2), 128–132.
26 B. Luhar, R. Dhankhar, R. V. Nair, A. Soni, N. S. Kamath, S. K. Pal and V. Balakrishnan, Charge transfer mediated photoluminescence engineering in WS_2 monolayers for optoelectronic application, *ACS Appl. Nano Mater.*, 2024, **7**(19), 22350–22359.
27 Y. Ge, W. Wan, W. Feng, D. Xiao and Y. Yao, Effect of doping and strain modulations on electron transport in monolayer MoS_2, *Phys. Rev. B:Condens. Matter Mater. Phys.*, 2014, **90**(3), 035414.
28 M. Buscema, G. A. Steele, H. S. J. van der Zant and A. Castellanos-Gomez, The effect of the substrate on the Raman and photoluminescence emission of single-layer MoS_2, *Nano Res.*, 2014, **7**(4), 561–571.
29 M. G. Harats, J. N. Kirchhof, M. Qiao, K. Greben and K. I. Bolotin, Dynamics and efficient conversion of excitons to trions in non-uniformly strained monolayer WS_2, *Nat. Photonics*, 2020, **14**(5), 324–329.
30 H. Kim, S. Z. Uddin, N. Higashitarumizu, E. Rabani and A. Javey, Inhibited nonradiative decay at all exciton densities in monolayer semiconductors, *Science*, 2021, **373**(6553), 448–452.
31 S. Z. Uddin, N. Higashitarumizu, H. Kim, J. Yi, X. Zhang, D. Chrzan and A. Javey, Enhanced neutral exciton diffusion in monolayer WS_2 by exciton–exciton annihilation, *ACS Nano*, 2022, **16**(5), 8005–8011.
32 A. Soni, N. S. Kamath, Y.-Y. Shen, H. Seksaria, A. De Sarkar, W.-H. Chang and S. K. Pal, Substrate-induced modulation of transient optical response of large-area monolayer MoS_2, *Sci. Rep.*, 2025, **15**(1), 7537.
33 A. Soni, S. Ghosal, M. Kundar, S. K. Pati and S. K. Pal, Long-lived interlayer excitons in WS_2/Ruddlesden–Popper perovskite van der Waals heterostructures, *ACS Appl. Mater. Interfaces*, 2024, **16**(27), 35841–35851.
34 G. Kresse and J. Furthmüller, Efficient iterative schemes for ab initio total-energy calculations using a plane-wave basis set, *Phys. Rev. B:Condens. Matter Mater. Phys.*, 1996, **54**(16), 11169–11186.
35 G. Kresse and J. Furthmüller, Efficiency of *ab initio* total energy calculations for metals and semiconductors using a plane-wave basis set, *Comput. Mater. Sci.*, 1996, **6**(1), 15–50.
36 J. P. Perdew, K. Burke and M. Ernzerhof, Generalized gradient approximation made simple, *Phys. Rev. Lett.*, 1996, **77**(18), 3865–3868.
37 P. E. Blöchl, Projector augmented-wave method, *Phys. Rev. B:Condens. Matter Mater. Phys.*, 1994, **50**(24), 17953–17979.
38 S. Grimme, J. Antony, S. Ehrlich and H. Krieg, A consistent and accurate ab initio parametrization of density functional dispersion correction (DFT-D) for the 94 elements H-Pu, *J. Chem. Phys.*, 2010, **132**(15), 154104.
39 S.-W. Kim, H.-J. Kim, S. Cheon and T.-H. Kim, Circular dichroism of emergent chiral stacking orders in quasi-one-dimensional charge density waves, *Phys. Rev. Lett.*, 2022, **128**(4), 046401.
40 U. Herath, P. Tavadze, X. He, E. Bousquet, S. Singh, F. Muñoz and A. H. Romero, PyProcar: A Python library for electronic structure pre/post-processing, *Comput. Phys. Commun.*, 2020, **251**, 107080.
41 A. Soni, D. Kushavah, L.-S. Lu, W.-H. Chang and S. K. Pal, Ultrafast exciton trapping and exciton–exciton annihilation in large-area CVD-grown monolayer WS_2, *J. Phys. Chem. C*, 2021, **125**(43), 23880–23888.
42 F. Wu, F. Qu and A. H. MacDonald, Exciton band structure of monolayer MoS_2, *Phys. Rev. B:Condens. Matter Mater. Phys.*, 2015, **91**(7), 075310.
43 I. C. Gerber, E. Courtade, S. Shree, C. Robert, T. Taniguchi, K. Watanabe, A. Balocchi, P. Renucci, D. Lagarde, X. Marie, *et al.*, Interlayer excitons in bilayer MoS_2 with strong oscillator strength up to room temperature, *Phys. Rev. B*, 2019, **99**(3), 035443.
44 H. Liu and D. Chi, Dispersive growth and laser-induced rippling of large-area singlelayer MoS_2 nanosheets by CVD on c-plane sapphire substrate, *Sci. Rep.*, 2015, **5**(1), 11756.
45 J. Mo, S. El Kazzi, W. Mortelmans, A. N. Mehta, S. Sergeant, Q. Smets, I. Asselberghs and C. Huyghebaert, Importance of the substrate's surface evolution during the MOVPE growth of 2D-transition metal dichalcogenides, *Nanotechnology*, 2020, **31**(12), 125604.
46 R. K. Prasad and D. K. Singh, Continuous large area monolayered molybdenum disulfide growth using atmospheric pressure chemical vapor deposition, *ACS Omega*, 2023, **8**(12), 10930–10940.
47 N. A. Lanzillo, A. Glen Birdwell, M. Amani, F. J. Crowne, P. B. Shah, S. Najmaei, Z. Liu, P. M. Ajayan, J. Lou, M. Dubey, *et al.*, Temperature-dependent phonon shifts in monolayer MoS_2, *Appl. Phys. Lett.*, 2013, **103**(9), 093102.
48 E. Mercado, A. Goodyear, J. Moffat, M. Cooke and R. S. Sundaram, A Raman metrology approach to quality control of 2D MoS_2 film fabrication, *J. Phys. D: Appl. Phys.*, 2017, **50**(18), 184005.
49 H. Li, Q. Zhang, C. C. R. Yap, B. K. Tay, T. H. T. Edwin, A. Olivier and D. Baillargeat, From bulk to monolayer

MoS_2: Evolution of Raman scattering, *Adv. Funct. Mater.*, 2012, **22**(7), 1385–1390.

50 K. Gołasa, M. Grzeszczyk, R. Bożek, P. Leszczyński, A. Wysmołek, M. Potemski and A. Babiński, Resonant Raman scattering in MoS_2—From bulk to monolayer, *Solid State Commun.*, 2014, **197**, 53–56.

51 Y.-T. Ho, C.-H. Ma, T.-T. Luong, L.-L. Wei, T.-C. Yen, W.-T. Hsu, W.-H. Chang, Y.-C. Chu, Y.-Y. Tu, K. P. Pande, *et al.*, Layered MoS_2 grown on c-sapphire by pulsed laser deposition, *Phys. Status Solidi RRL*, 2015, **9**(3), 187–191.

52 L. Kang, D. Tian, L. Meng, M. Du, W. Yan, Z. Meng and X.-a. Li, Epitaxial growth of highly-aligned MoS_2 on c-plane sapphire, *Surf. Sci.*, 2022, **720**, 122046.

53 J. W. Christopher, B. B. Goldberg and A. K. Swan, Long tailed trions in monolayer MoS_2: Temperature dependent asymmetry and resulting red-shift of trion photoluminescence spectra, *Sci. Rep.*, 2017, **7**(1), 14062.

54 P. K. Mohapatra, S. Deb, B. P. Singh, P. Vasa and S. Dhar, Strictly monolayer large continuous MoS_2 films on diverse substrates and their luminescence properties, *Appl. Phys. Lett.*, 2016, **108**(4), 042101.

55 P. Hu, J. Ye, X. He, K. Du, K. K. Zhang, X. Wang, Q. Xiong, Z. Liu, H. Jiang and C. Kloc, Control of radiative exciton recombination by charge transfer induced surface dipoles in MoS_2 and WS_2 monolayers, *Sci. Rep.*, 2016, **6**(1), 24105.

56 X. Fan, D. J. Singh and W. Zheng, Valence band splitting on multilayer MoS_2: Mixing of spin–orbit coupling and interlayer coupling, *J. Phys. Chem. Lett.*, 2016, **7**(12), 2175–2181.

57 S.-D. Guo, Spin–orbit and strain effect on power factor in monolayer MoS_2, *Comput. Mater. Sci.*, 2016, **123**, 8–13.

58 I. Demeridou, A. Papadopoulos, G. Kourmoulakis, L. Mouchliadis, E. Stratakis and G. Kioseoglou, Tuning the valley polarization in WS_2 monolayers via control of active defect sites induced by photochemical doping, *Appl. Phys. Lett.*, 2021, **118**(12), 123103.

59 M. Z. Maialle, E. A. de Andrada e Silva and L. J. Sham, Exciton spin dynamics in quantum wells, *Phys. Rev. B: Condens. Matter Mater. Phys.*, 1993, **47**(23), 15776–15788.

60 A. M. Jones, H. Yu, N. J. Ghimire, S. Wu, G. Aivazian, J. S. Ross, B. Zhao, J. Yan, D. G. Mandrus, D. Xiao, *et al.*, Optical generation of excitonic valley coherence in monolayer WSe_2, *Nat. Nanotechnol.*, 2013, **8**(9), 634–638.

61 G. Kioseoglou, A. T. Hanbicki, M. Currie, A. L. Friedman, D. Gunlycke and B. T. Jonker, Valley polarization and intervalley scattering in monolayer MoS_2, *Appl. Phys. Lett.*, 2012, **101**(22), 221907.

62 D. Lagarde, L. Bouet, X. Marie, C. R. Zhu, B. L. Liu, T. Amand, P. H. Tan and B. Urbaszek, Carrier and polarization dynamics in monolayer MoS_2, *Phys. Rev. Lett.*, 2014, **112**(4), 047401.

63 X.-T. An, J. Xiao, M. W. Y. Tu, H. Yu, V. I. Fal'ko and W. Yao, Realization of valley and spin pumps by scattering at nonmagnetic disorders, *Phys. Rev. Lett.*, 2017, **118**(9), 096602.

64 A. Singh, K. Tran, M. Kolarczik, J. Seifert, Y. Wang, K. Hao, D. Pleskot, N. M. Gabor, S. Helmrich, N. Owschimikow, *et al.*, Long-lived valley polarization of intravalley trions in monolayer WSe_2, *Phys. Rev. Lett.*, 2016, **117**(25), 257402.

65 Q. Zhang, H. Sun, J. Tang, X. Dai, Z. Wang and C.-Z. Ning, Prolonging valley polarization lifetime through gate-controlled exciton-to-trion conversion in monolayer molybdenum ditelluride, *Nat. Commun.*, 2022, **13**(1), 4101.

66 K. Hao, L. Xu, F. Wu, P. Nagler, K. Tran, X. Ma, C. Schüller, T. Korn, A. H. MacDonald, G. Moody, *et al.*, Trion valley coherence in monolayer semiconductors, *2D Mater.*, 2017, **4**(2), 025105.

67 J. Pu, W. Zhang, H. Matsuoka, Y. Kobayashi, Y. Takaguchi, Y. Miyata, K. Matsuda, Y. Miyauchi and T. Takenobu, Room-temperature chiral light-emitting diode based on strained monolayer semiconductors, *Adv. Mater.*, 2021, **33**(36), 2100601.

68 F. Xia, H. Wang, D. Xiao, M. Dubey and A. Ramasubramaniam, Two-dimensional material nanophotonics, *Nat. Photonics*, 2014, **8**(12), 899–907.

69 S. Yang, H. Long, W. Chen, B. Sa, Z. Guo, J. Zheng, J. Pei, H. Zhan and Y. Lu, Valleytronics meets straintronics: Valley fine structure engineering of 2D transition metal dichalcogenides, *Adv. Opt. Mater.*, 2024, **12**(14), 2302900.

70 H. Tian, C. Ren and S. Wang, Valleytronics in two-dimensional materials with line defect, *Nanotechnology*, 2022, **33**(21), 212001.

71 Y. Liu, Y. Gao, S. Zhang, J. He, J. Yu and Z. Liu, Valleytronics in transition metal dichalcogenides materials, *Nano Res.*, 2019, **12**(11), 2695–2711.

72 D. J. Thouless, M. Kohmoto, M. P. Nightingale and M. den Nijs, Quantized Hall conductance in a two-dimensional periodic potential, *Phys. Rev. Lett.*, 1982, **49**(6), 405–408.

73 M. Gradhand, D. V. Fedorov, F. Pientka, P. Zahn, I. Mertig and B. L. Györffy, First-principles calculations of the Berry curvature of Bloch states for charge and spin transport of electrons, *J. Phys.: Condens. Matter*, 2012, **24**(21), 213202.

74 H.-J. Kim, C. Li, J. Feng, J.-H. Cho and Z. Zhang, Competing magnetic orderings and tunable topological states in two-dimensional hexagonal organometallic lattices, *Phys. Rev. B*, 2016, **93**(4), 041404.

75 Transition (dipole) moment, in *IUPAC Compendium of Chemical Terminology*, International Union of Pure and Applied Chemistry, 5th edn, 2025. Online version 5.0.0, 2025.